Chapter 8
Various Physical and Chemical Properties of Lotus Metals

Abstract Lotus metals have anisotropic pore configuration. Such anisotropic pores yield anisotropic behavior of sound absorption, electrical and thermal conductivity, magnetization, and corrosion behavior, because the pore itself affects those materials characteristics. However, it does not affect thermal expansion, because only nonporous body controls thermal expansion. Thus, lotus metals exhibit unique characteristics.

Keywords Corrosion • Magnetization • Sound absorption • Thermal conductivity • Thermal expansion

8.1 Sound Absorption

Sound absorption materials with an advanced performance to noises are required for mufflers of cars, air-conditioner parts, pump chambers, elevated roads, etc. The glass wool and foamed aluminum with closed pores are used most frequently as marketed sound-absorbing materials at present. In most cases, these materials have low strength, though they have good sound absorption capacity. The development of the sound-absorbing material with comprehensive characteristics such as high strength, lightweight, and good sound absorption capacity is desirable. In order to investigate whether lotus metals exhibit significant sound absorption characteristics, Xie et al. [1–3] measured the sound absorption coefficient of lotus magnesium and copper plates by standing-wave method [4]. It is well known that the absorption coefficient depends on the angle between the material surface and the incident sound wave. In the experiments, the specimen surface was set perpendicular to the incident sound wave. Figure 8.1 shows the schematic drawing for measurements of the sound absorption coefficient. The specimen was set on the rigid wall in the sound tube. A pure sound with a single frequency was generated from the speaker installed at the other end. The standing-wave is caused by the interference between an incidence wave and a reflection wave in the tube.

H. Nakajima, *Porous Metals with Directional Pores*,
DOI 10.1007/978-4-431-54017-5_8, © Springer Japan 2013

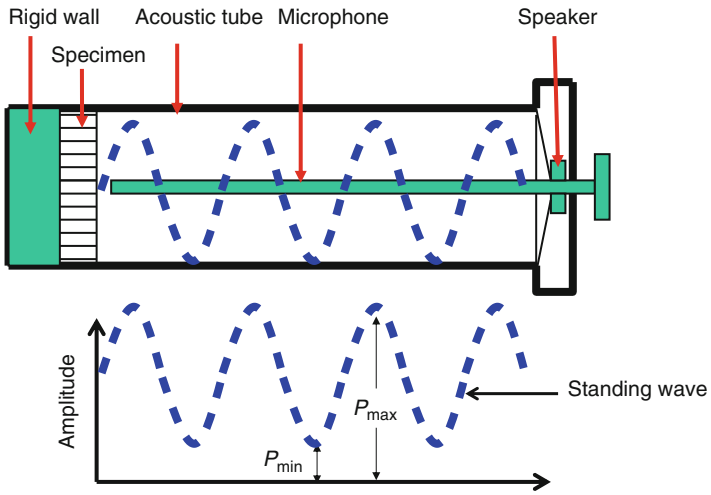

Fig. 8.1 Schematic drawings for measurement of sound absorption coefficient by standing-wave method

The sound pressure becomes the maximum at each quarter of the wavelength. The maximum value of the sound pressure is written as $|p|_{\max} = |A + B|$, where A and B are the amplitude of incidence wave and reflection wave, respectively. The minimum value of the sound pressure is written as $|p|_{\min} = |A - B|$. The ratio between the maximum and minimum of the sound pressure, n, is given by

$$\frac{|p|_{\max}}{|p|_{\min}} = \frac{|A + B|}{|A - B|} = n. \tag{8.1}$$

The sound reflectivity of the specimen is written as

$$|r_p| = \left|\frac{B}{A}\right| = \frac{n - 1}{n + 1}. \tag{8.2}$$

The absorption coefficient, α_0, is given by

$$\alpha_0 = 1 - |r_p|^2 = \frac{4}{n + (1/n) + 2}. \tag{8.3}$$

$|p|_{\max}$ and $|p|_{\min}$ are measured by moving the microphone in the tube to determine the value of n. Then the absorption coefficient can be calculated using Eq. (8.3). This measuring method is called a standing-wave method, which is one of the tube methods, and the details are provided in JIS A 1405–1963 standards [4].

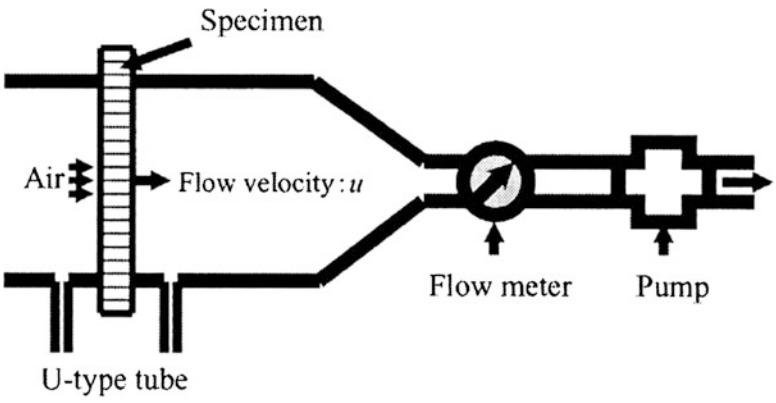

Fig. 8.2 Schematic drawing for measurement of flow resistance (Reprinted with permission from [1] © 2004 Elsevier B.V.)

Both the flow resistance and the absorption coefficient show amount of the performance of absorbing sound in the porous material. Therefore, it is necessary to measure the flow resistance of the lotus copper. The flow resistance of the sound-absorbing material is basically the same as the ventilation resistance, used to show the ventilations such as cloth and paper. Unit area flow resistance of the porous sound-absorbing material is defined by

$$R_f = \frac{\Delta p}{u}, \tag{8.4}$$

where u is the flow ratio when the constant air is passed through the vertical direction on the surface of the material and Δp is the difference in pressure at both sides of material. A pump is operated as shown in Fig. 8.2, and the differential pressure between both sides of the specimen is measured with a U manometer. The flow ratio u is written as

$$u = \frac{Q}{S}, \tag{8.5}$$

where S and Q are area of specimen and flow volume of air, respectively.

Zie et al. measured the absorption coefficients α_0 for the lotus copper as a function of pore diameter under the condition that the specimen thickness and the porosity were constant [1]. As shown in Fig. 8.3, α_0 increases with decrease in pore diameter from 660 to 460 μm in the whole frequency range up to 4 kHz. Figure 8.4 shows the porosity dependence of the absorption coefficient for constant pore diameter 380 μm and constant specimen thickness 10 mm. The absorption coefficient increases with increasing porosity from 43 to 62 %. There are some data scattering, which is attributed to coexistence of non-permeable and permeable pores. Figure 8.5 shows the dependence of the absorption coefficient on specimen

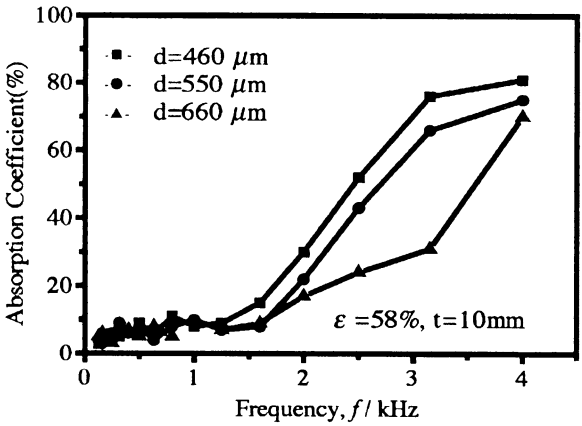

Fig. 8.3 Effect of pore diameter on sound absorption coefficient of lotus copper (Reprinted with permission from [1] © 2004 Elsevier B.V.)

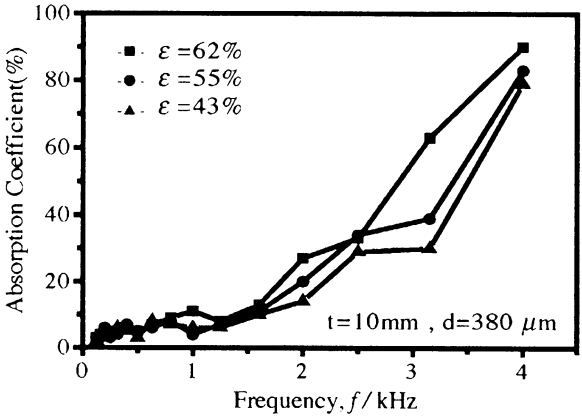

Fig. 8.4 Effect of porosity on sound absorption coefficient of lotus copper (Reprinted with permission from [1] © 2004 Elsevier B.V.)

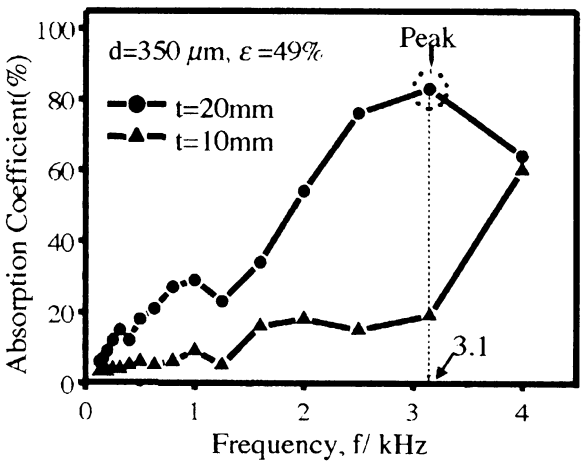

Fig. 8.5 Effect of specimen thickness with 10 and 20 mm on sound absorption coefficient of lotus copper (Reprinted with permission from [1] © 2004 Elsevier B.V.)

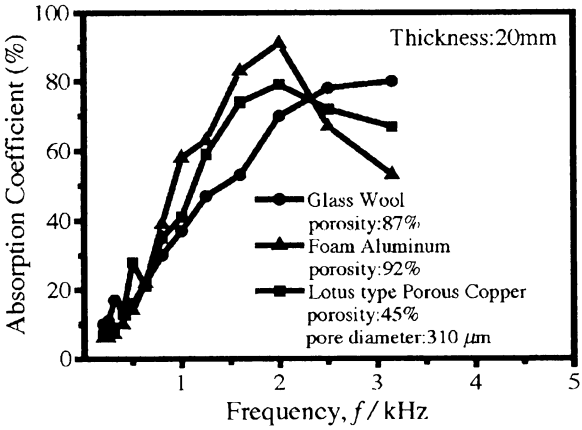

Fig. 8.6 Comparison of absorption coefficient of various materials (Reprinted with permission from [1] © 2004 Elsevier B.V.)

thickness when the pore diameter and porosity are constant. The absorption coefficient increases with increasing thickness. Especially, the absorption coefficient increases significantly in high-frequency range. The maximum of α_0 was observed at 3.1 kHz in the specimen of 20 mm thick, while such maximum value was not found until 4 kHz in the specimen of 10 mm thick. A similar tendency was observed for lotus magnesium [5].

The glass wool has a peculiar mechanism of absorbing sound and is used widely as the sound-absorbing material. The absorption coefficients of lotus copper, the foam aluminum, and the glass wool with the same thickness, in the same frequency region, were compared as shown in Fig. 8.6. All of them were measured by a standard-wave method. The glass wool [6] and foam aluminum [7] exhibit superior absorption capacity. The foam aluminum is composed of many independent closed pores. Continuous pores are necessary to have high-sound absorption capacity [6] so that minute cracks are introduced by rolling to connect the pores of the foam aluminum.

For mechanism of sound absorption, it is thought that the viscosity resistance of air in pores plays an important role in absorbing the sound for the porous material. The sound is absorbed by the resistance in the fiber and this space of pores, when the sound enters into the open pores in porous materials [8]. The sound is also absorbed by disturbance of the movement of air. The absorption of the sound in porous material is considered to be mainly due to the consumption of the sound energy by the viscosity and the thermal conduction when the sound is propagating into this tube. It is difficult to analyze this strictly because the pores in the porous material are arranged to have complex shape.

The lotus metal can be considered as an assembly of many parallel thin tubes. In order to simplify the analysis, first consider how a sound propagates in only one tube. When a sound propagates in a thin tube, the attenuation of a sound depends on the material of the tube. The attenuation in a smooth metal tube has been reported to be larger than the attenuation in air [9]. According to Igarasi [10], the attenuation constant β is expressed as

$$\beta = \frac{0.0102}{cr} f^{1/2}, \tag{8.6}$$

where c and r are speed of sound and radius of tube, respectively. The attenuation of sound can often be disregarded when the inner diameter exceeds several centimeters because attenuation is reversely proportional to the inner diameter in Eq. (8.6). On the other hand, since the radius of pores of the lotus copper is from 200 μm to 1 mm, the attenuation increases when the sound enters lotus copper. The attenuation constants of N pores are given by

$$\beta_N = \frac{\beta}{N} = \frac{0.0102}{crN} f^{1/2}. \tag{8.7}$$

The relation between the pore number and the porosity is written as

$$N = \frac{r_1^2 \varepsilon}{r^2}, \tag{8.8}$$

where r_1 is a radius of the specimen. From Eqs. (8.7) and (8.8), the attenuation constant in the lotus copper is given by

$$\beta_N = \frac{0.0102}{c\varepsilon r_1^2} f^{1/2}. \tag{8.9}$$

It is thought that the reason of absorbing sound is mainly due to viscous friction of air in the lotus copper. The absorption effect by only permeable pores is taken into consideration. Therefore, it is necessary to measure the porosity of only permeable pores. The thicker the specimen is, the more pores become difficult to be permeable because the length of elongated pores is limited in the lotus copper. It has been known that the pores are hardly permeable in the specimen of 20 mm or more in thickness. Therefore, some differences were seen in the absorption coefficient–frequency curve when the porosity was increased from 43 to 62 % in Fig. 8.4.

The attenuation mechanism of the lotus copper is considered to be the change of absorption sound energy into thermal energy by the viscous friction in the pores. From this viewpoint, the attenuation constant in the lotus copper is related to the radius, the porosity, the pore diameter, the thickness of the specimen, and the frequency. Figure 8.7 shows the relation of the absorption coefficient and attenuation constant by calculating from Eq. (8.9). Thus, it is found that the absorption coefficient is related to the attenuation constant of the specimen.

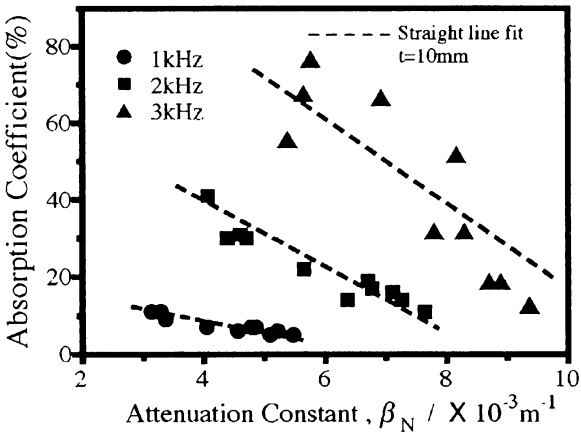

Fig. 8.7 A relation between absorption coefficient and attenuation constant of lotus copper with 10-mm thickness (Reprinted with permission from [1] © 2004 Elsevier B.V.)

8.2 Thermal Conductivity

To use lotus copper effectively as heat sinks mentioned later, it is very important to know its effective thermal conductivity and consider the pore effect on the heat flow. There is much in the literatures devoted to the effective thermal conductivity of composite materials with cylindrical inclusions. Behrens [11] analytically investigated the effective thermal conductivities of composite materials under the assumption of orthorhombic symmetry and proposed a simple equation for predicting the effective thermal conductivity. Perrin et al. [12] proposed a method for predicting transport properties that included the thermal conductivity of circular cylinders in square and hexagonal arrays. Han and Cosner [13] concluded a numerical investigation of the effective thermal conductivities of composites with uniform fibers in unidirectional orientation and layered composites with fibers laid alternately along two mutually perpendicular directions. A numerical method was devoted by Sangani and Yao [14] to determine the effective thermal conductivity of a composite medium consisting of parallel circular cylinders in random arrays. They cited that the conductivity appeared to be a relatively weak function of the detailed arrangement of the cylinders. Mityushev [15] extended analysis of the resolution of the Laplace equation in composite material with a collection of non-overlapping, identical, circular disks. Moctezuma-Berthier et al. [16] showed the predominant influence of the total porosity on the thermal properties of vulgar porous media. Ogushi et al. [17] investigated the effective thermal conductivities parallel and perpendicular to the pore axis of lotus copper both experimentally and analytically. Since the thermal conductivity of the fluid in the pores is negligible in comparison to lotus copper material in the application of lotus copper to heat sinks, a very simple equation can describe the thermal conductivities of lotus copper.

8.2.1 Measurement of Effective Thermal Conductivity of Lotus Copper

The effective thermal conductivity of lotus copper k_{eff} is defined by

$$q = \frac{Q}{A} = -k_{\text{eff}} \nabla T, \tag{8.10}$$

where q is the heat flux from heat flow Q divided by heat flowing through the cross-sectional area A in lotus copper including the pores, and T is the temperature in lotus copper. The tensor k_{eff} is orthorhombic and is expressed as

$$k_{\text{eff}} = \begin{pmatrix} k_{\text{eff}\parallel} & & \\ & k_{\text{eff}} & \\ & & k_{\text{eff}} \end{pmatrix}. \tag{8.11}$$

The effective thermal conductivity of lotus copper is anisotropic. The parallel and perpendicular effective thermal conductivities, $k_{\text{eff}//}$ and $k_{\text{eff}\perp}$, of lotus copper are defined as the thermal conductivities for heat flow parallel and perpendicular to the pore axis, respectively.

Figure 8.8 presents the experimental apparatus for measuring the effective thermal conductivity. A cylindrical specimen with a diameter of 30 mm and a length of 30 mm was located between upper and lower copper rods of known thermal conductivity. The upper rod was heated by electrical heaters from the top surface, while the bottom surface of the lower rod was cooled by cooling water in order to transmit a certain amount of heat through the specimen. K-type thermocouples were located each at 5-mm spacing in the specimen and the upper and the lower rods to measure the temperature. An example of the temperature distribution of the experimental setup is shown in Fig. 8.9. As the heat flowed in one direction through the rods and specimen from top to bottom, heat flux q through the specimen was obtained by the following one-dimensional equations:

$$q = \frac{q_1 + q_2}{2}, \tag{8.12}$$

$$q_1 = -k_{\text{Cu}} \left(\frac{\partial T}{\partial x} \right)_1, \tag{8.13}$$

$$q_2 = -k_{\text{Cu}} \left(\frac{\partial T}{\partial x} \right)_2, \tag{8.14}$$

where q_1 is a heat flux from the upper rod to the specimen and q_2 is the heat flux from the specimen to the lower rod, k_{Cu} is the thermal conductivity of the rod, and x is the direction of heat flow from the upper to the lower rod. From

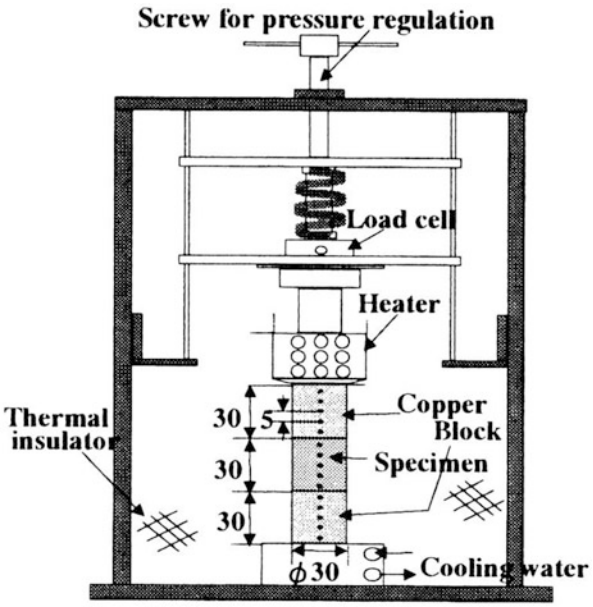

Fig. 8.8 Experimental apparatus for measuring effective thermal conductivity (Reprinted with permission from [17] © 2004 American Institute of Physics)

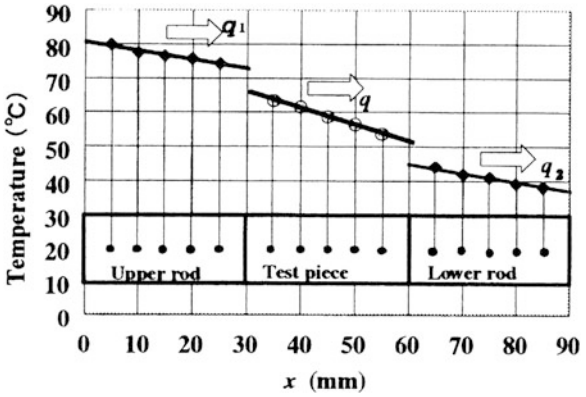

Fig. 8.9 Temperature distribution in specimen and rods (Reprinted with permission from [17] © 2004 American Institute of Physics)

Eqs. (8.10)–(8.14), effective thermal conductivity $k_{\text{eff}//}$ and $k_{\text{eff}\perp}$ are obtained by the following equation:

$$k_{\text{eff}||}, \quad k_{\text{eff}\perp} = -\frac{q_1 + q_2}{2\left(\frac{\partial T}{\partial x}\right)_{\text{lotus}}}, \tag{8.15}$$

where $(\partial T/\partial x)_{\text{lotus}}$ is the temperature gradient in the specimen with pores parallel or perpendicular to heat flow direction x.

8.2.2 Analysis of Effective Thermal Conductivity of Lotus Copper

Since the heat flow cross-sectional areas parallel to the pore axis in lotus copper is proportional to $(1-\varepsilon)$, the effective thermal conductivity $k_{\text{eff}//}$ is expressed by the following equation:

$$\frac{k_{\text{eff}||}}{k_s} = 1 - \varepsilon, \tag{8.16}$$

where k_s is the thermal conductivity of nonporous copper and ε is the porosity expressed by the volume ratio of pores versus the total volume of lotus copper.

Behrens [11] derived the effective thermal conductivity of composite materials with orthorhombic symmetry. By applying his equation to the thermal conductivity of lotus copper, the effective thermal conductivity perpendicular to the pores can be expressed by the following equation:

$$\frac{k_{\text{eff}\perp}}{k_s} = \frac{(\beta+1)+\varepsilon(\beta-1)}{(\beta+1)-\varepsilon(\beta-1)}, \tag{8.17}$$

where $\beta(=k_p/k_s)$ is the conductivity ratio, that is, pore conductivity k_p divided by material conductivity k_s of lotus copper. Because the thermal conductivity of the hydrogen gas or air in the pores of lotus copper is negligible compared with that of lotus material, the effective thermal conductivity of lotus copper is derived as the following equation by setting $\beta = 0$ in the above equation:

$$\frac{k_{\text{eff}\perp}}{k_s} = \frac{1-\varepsilon}{1+\varepsilon}. \tag{8.18}$$

Han and Cosner [13] performed a numerical study on the effective thermal conductivities of fibrous composites using a unit-cell approach under a uniform fiber diameter condition. Since the diameter of lotus copper is distributed around a certain range, numerical simulation for the thermal conductivity perpendicular to the pores under a nonuniform pore diameter condition was conducted to verify the applicability of Eq. (8.18) to lotus copper.

Figure 8.10a shows a comparison between the experimental data and the results evaluated by the analytical equation, Eq. (8.16), for thermal conductivity parallel to the pores. Experimental data for $k_{\text{eff}//}$ showed good agreement with the analytical results derived from the assumption that heat flow through the cross-sectional area parallel to the pore axis is proportional to $(1-\varepsilon)$. A value of 335 W/(mK) for thermal conductivity k_s of the lotus copper material was used for comparison. Figure 8.10b gives a comparison between the experimental data and Eq. (8.18), where effective thermal conductivity $k_{\text{eff}\perp}$ perpendicular to the pores was lower than that of the parallel ones($k_{\text{eff}//}$) and was 40 % of lotus copper material k_s with a

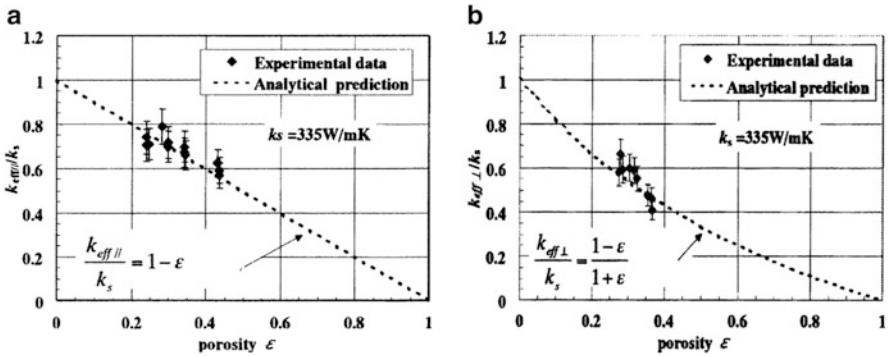

Fig. 8.10 (**a**) Comparison of experimental data of the effective thermal conductivity of lotus copper parallel to pores with analysis data. (**b**) Comparison of experimental results of the effective thermal conductivity of lotus copper perpendicular to pores with analysis data (Reprinted with permission from [17] © 2004 American Institute of Physics)

porosity of 0.4. The analytical values evaluated by Eq. (8.18) showed good agreement with the experimental data, indicating that Eq. (8.18) can be used to predict the effective thermal conductivity perpendicular to pores of lotus copper within experimental accuracy of ±10 %. The results show that lotus copper displayed anisotropy of the effective thermal conductivity. The effective thermal conductivity $k_{\mathrm{eff}\perp}$ perpendicular to pores was lower than that of parallel to $k_{\mathrm{eff}//}$ ones.

8.3 Electrical Conductivity

For the permeability and large surface area, porous metals are indispensable as electrode materials of a battery. The conventional porous electrode materials are fabricated with powder metallurgy, and therefore the porous structure is complicated, i.e., the pores are nonuniform and dispersed irregularly. This complicated structure results in a degradation of the strength and permeability of the electrolyte solution. Because of this unique porous structure of the directional porosity metals, lotus metals show more superior mechanical properties than the conventional porous metals [18]. Suematsu et al. [19] succeeded to fabricate lotus nickel; this porous nickel is promising as a new type of electrode material that possesses the superior strength and permeability. For this application, the effect of pore structure and porosity on the electrical conductivity needs to be investigated. Thus, Tane et al. [20] studied the electrical conductivity of lotus-type porous nickel. The first part describes the experimental result on the conductivity parallel and perpendicular to the longitudinal pore directions measured by four-probe method. Next, a calculation method is shown for the electrical conductivity of such an anisotropic porous structure on the basis of the effective-mean-field (EMF) theory [21]. Finally the validity of the calculation by the method is discussed, comparing with the measurement data.

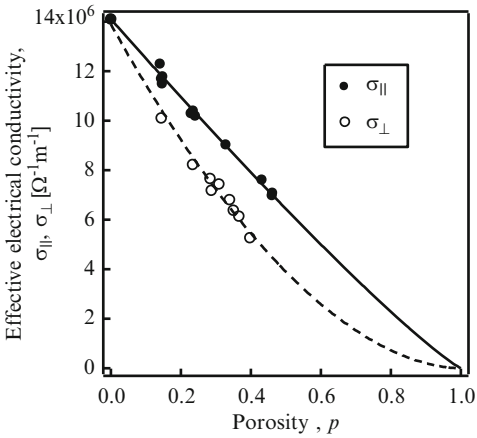

Fig. 8.11 Porosity dependence of the electrical conductivity of lotus nickel. The *plots* indicate measured result, and the *lines* indicate fitting the equation to the measurements (Reprinted with permission from [20] © 2005 American Institute of Physics)

8.3.1 Measurement of Electrical Conductivity of Lotus Nickel

Lotus nickel ingots with long straight pores aligned in one direction were fabricated through unidirectional solidification in a pressurized hydrogen or argon gas. Continuous current electrical conductivity along the longitudinal direction of the specimen was measured with the four-probe method at room temperature.

Figure 8.11 shows the porosity dependence of the normalized effective electrical conductivities $\sigma_{\parallel}/\sigma_0$ and $\sigma_{\perp}/\sigma_0$, where $\sigma_{\parallel}/\sigma_0$ and $\sigma_{\perp}/\sigma_0$ denote the normalized effective electrical conductivity parallel and perpendicular to the longitudinal pore direction, respectively. The electrical conductivity of nonporous material, σ_0, is $1.41 \times 10^7\ \Omega^{-1}\ \mathrm{m}^{-1}$. The electrical conductivity shows the anisotropy that reflects the porous structure. For the parallel to the longitudinal pore direction, the specific conductivity is almost retained. This is because the flow direction of the electrical current in the nickel matrix is almost parallel to the applied electric field. For the perpendicular direction, the electrical current needs to flow detouring around pores. Therefore, a distance that the electrical current flows increases, which results in the increase of the effective electrical resistivity (decrease of the effective electrical conductivity).

8.3.2 Analysis of Electrical Conductivity of Lotus Nickel

The previous extensive researches about porous rocks elucidated that porosity dependence of the effective conductivity follows an empirical formula (called Archie's law [22]):

$$\sigma = \sigma_0(1-p)^m, \tag{8.19}$$

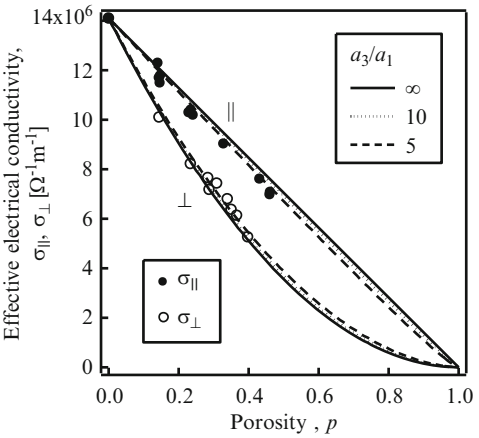

Fig. 8.12 Porosity dependence of the effective electrical conductivity of lotus nickel parallel and perpendicular to the pore growth direction in the case of $a_3/a_1 = 5$, 10, and ∞, which are calculated with EMF theory. *Plots* indicate the measurement data, and *lines* indicate the calculation results with EMF theory (Reprinted with permission from [20] © 2005 American Institute of Physics)

where σ and σ_0 are the effective electrical conductivity of porous and nonporous material, respectively, and m is the coefficient determined empirically. Eq. (8.19) was fitted to the measurement data, and lines in Fig. 8.11 show the fitting curves. It is found that power-law relation holds in the anisotropic porous metals. The coefficient m for parallel and perpendicular conductivity is estimated at 1.1 and 1.8, respectively.

Tane et al. [20] applied the concept of EMF theory to derive the effective electrical conductivity of composites. Composites consist of the matrix and one type of inclusions, whose volume fractions are denoted by f_M and $f_I (= 1 - f_M)$, respectively. Spatial averages of an electrical current density $\overline{\mathbf{J}}$ (3×1 vector) and electric field $\overline{\mathbf{E}}$ (3×1 vector) of composites are expressed as $\overline{\mathbf{J}} = f_M \overline{\mathbf{J}}_M + f_I \overline{\mathbf{J}}_I$ and $\overline{\mathbf{E}} = f_M \overline{\mathbf{E}}_M + f_I \overline{\mathbf{E}}_I$, where $\overline{\mathbf{J}}_M = \sigma_M \overline{\mathbf{E}}_M$ and $\overline{\mathbf{J}}_I = \sigma_I \overline{\mathbf{E}}_I$ and σ_M and σ_I are electrical conductivity of matrix and inclusion, respectively (σ is 3×3 matrix, and the component is 0 when $i \neq j$). The electric field $\mathbf{E}$ is defined as $\mathbf{E} = -\mathbf{grad}\phi$, where ϕ is the electric potential. Then, the effective electrical conductivity $\overline{\sigma}$ of the composites are defined as $\overline{\mathbf{J}} = \overline{\sigma}\overline{\mathbf{E}}$. When expressing $\overline{\mathbf{E}}_I = \mathbf{A}\,\overline{\mathbf{E}}_M$, the effective electrical conductivity $\overline{\sigma}$ of the composite can be written as

$$\overline{\sigma} = (f_M \sigma_M + f_I \sigma_I \mathbf{A})[f_M \mathbf{I} + f_I \mathbf{A}]^{-1}, \tag{8.20}$$

where $\mathbf{I}$ is the unit matrix (3×3 matrix). Using Eshelby's equivalent inclusion theory [23] and mean-field theory [24], $\mathbf{A}$ (3×3 matrix) can be expressed as $\mathbf{A} = [\mathbf{S}\sigma_M^{-1}(\sigma_I - \sigma_M) + \mathbf{I}]^{-1}$ in analogy with the elasticity problem [25]. $\mathbf{S}$ is the 2nd-rank Eshelby tensor.

When the present EMF theory is applied to lotus nickel, we assumed that the pore shape is ellipsoidal of $a_1 = a_2$, and the electric conductivity for the pore σ_I is 0, where a_1, a_2, and a_3 denote the radii of the ellipsoidal inclusion. Figure 8.12 shows the porosity dependence of $\sigma_{\parallel}/\sigma_0$ and $\sigma_{\perp}/\sigma_0$ in the case of $a_3/a_1 = 5, 10$

and ∞. Measurement data are shown for comparison. Practical a_3/a_1 of lotus nickel is 5–10 [26], and in this range the calculations agree well with the measurements. Furthermore, the calculation can fully simulate the power-law formula. When $a_3/a_1 \rightarrow \infty$, i.e., in the case of typical lotus metal, the effective electrical conductivities parallel and perpendicular to the longitudinal pore direction are expressed with the power-law formula:

$$\left.\begin{aligned} \sigma_{\parallel} &= \sigma_0(1-p)^1, \\ \sigma_{\perp} &= \sigma_0(1-p)^2. \end{aligned}\right\} \tag{8.21}$$

The electrical conductivity of lotus nickel with cylindrical pores aligned unidirectionally was measured. It is found that lotus nickel shows the anisotropy in the electrical conductivity because of the anisotropic porous structure; the effective conductivity parallel to longitudinal pore direction decreases linearly, while that perpendicular to the pore direction decreases steeply. These porosity dependencies follow Archie's power-law formula. The electrical conductivity of lotus nickel calculated with this theory is consistent with measurement data, and the EMF theory can fully simulate Archie's power-law formula.

8.4 Magnetization

In the application of lotus materials to magnetic materials, lotus materials are expected to have a useful merit that the geometrical magnetic anisotropy, called shape magnetic anisotropy, can be controlled by the growth direction of pores, without any change in the outer shape of material. For example, although the perpendicular direction of platelike samples is a hard axis of magnetization, it is possible to make the perpendicular direction be an easy axis of magnetization by introducing elongated pores aligned perpendicular to the plate. With regard to magnetic properties of porous materials, the effect of pore size has been widely studied for materials possessing isotropic pores [27, 28], but lotus materials have never been investigated. Onishi et al. [29] measured magnetization curves of lotus nickel and cobalt to characterize the anisotropy of the magnetization process, and the effect of porosity on the anisotropy was analyzed in terms of the empirical Archie's law.

The saturation magnetization of the porous and nonporous specimens was measured in the magnetic fields applied parallel and perpendicular to the pore growth direction. Due to the fact that the magnitudes of saturation magnetization of normal ferromagnetic materials such as nickel are given by the atomistic origin, it does not depend on the shapes of specimens and the directions of applied magnetic field, and it was confirmed that the saturation magnetization observed for porous nickel decreased linearly with increasing porosity. The same behavior was observed for cobalt. The relationship between the saturation magnetization of porous nickel and cobalt and their porosities is summarized in Fig. 8.13. The ratios

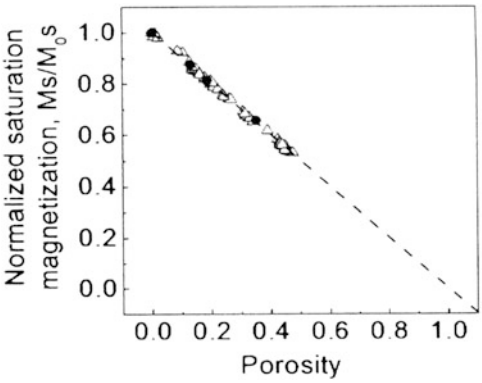

Fig. 8.13 Porosity dependence of the normalized saturation magnetization (M_{sat}/M_{0sat}) of lotus nickel (*filled circles*) and cobalt (*triangles*) (Reprinted with permission from [29] © 2008 American Institute of Physics)

of the saturation magnetization of the porous materials to that of the nonporous material naturally correspond with the volume ratios of the net metal to the whole porous material $(1-p)$ [30]. As a result, the saturation magnetization of porous materials is expressed by the following formula:

$$M_{sat} = M_{0sat}(1-p), \tag{8.22}$$

where M_{sat} and M_{0sat} denote the saturation magnetization of the porous material and that of the nonporous material, respectively. This result shows that the porosity of a porous material can be estimated easily by comparing its saturation magnetization with that of nonporous material.

Next, the magnetic field dependence of magnetization was in detail measured for the lotus nickel and cobalt. Although there is no remarkable difference in the obtained results between nickel and cobalt, effects of the pore direction are clearer in nickel. This is due to the soft magnetic properties of nickel. Figure 8.14a, b shows the normalized magnetization curves if lotus nickel, i.e., the magnetic field dependence of the ratio of the magnetization of porous specimens (M) to their saturation magnetization (M_{sat}), in the magnetic field parallel and perpendicular to the pore growth direction. It was observed that for all the cases, the M/M_{sat} values were close to unity above 3 kOe, showing the nearly saturated state. When the magnetic field was applied parallel to the pore growth direction, the normalized magnetization curve of the porous specimen corresponded with that of the nonporous specimen, as shown in Fig. 8.14a. In the case of perpendicular direction, on the other hand, different slopes of the normalized magnetization curves appeared at low-magnetic fields and the M/M_{sat} value decreased with the increase in the porosity as shown in Fig. 8.14b. The different slopes between the parallel and perpendicular directions were caused by geometric magnetic anisotropy of specimens containing anisotropic pores. In Fig. 8.15, M was normalized against the magnetization of the nonporous specimen (M_0) in order to discuss the porosity dependence of the magnitude of anisotropy in terms of Archie's formula. Only in the case of the magnetization perpendicular to the pore growth direction, significant lowering of the M/M_0 was

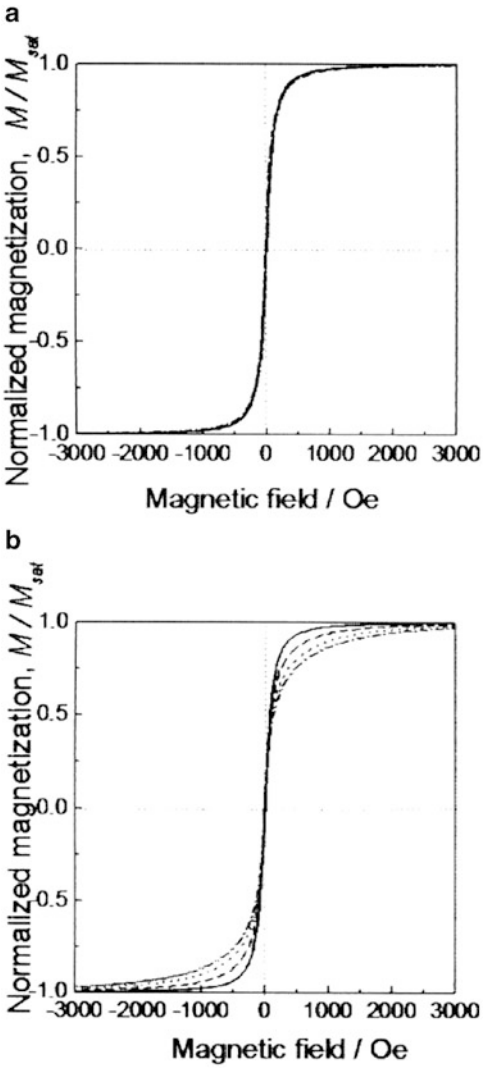

Fig. 8.14 Magnetization curves for specimens of 0 % porosity (*solid line*), 11 % porosity (*broken line*), 19 % porosity, and 35 % porosity (*chain line*) in the low-magnetic field (**a**) parallel and (**b**) perpendicular to the pore growth direction (Reprinted with permission from [29] © 2008 American Institute of Physics)

observed, at the low-magnetic field of ~200 Oe and was enhanced with increasing porosity. The relationship between the porosity and M/M_0 at a low- magnetic field (~200 Oe), an intermediate magnetic field (~1 kOe), and a high-magnetic field (~10 kOe) were shown in Fig. 8.16a–c, respectively. The relationship for the cases could be fitted by the following Archie's law:

$$M = M_0(1-p)^n, \tag{8.23}$$

where the exponent n is a fitting parameter. In this equation, it is considered that difference between parallel and perpendicular directions represents the relationship

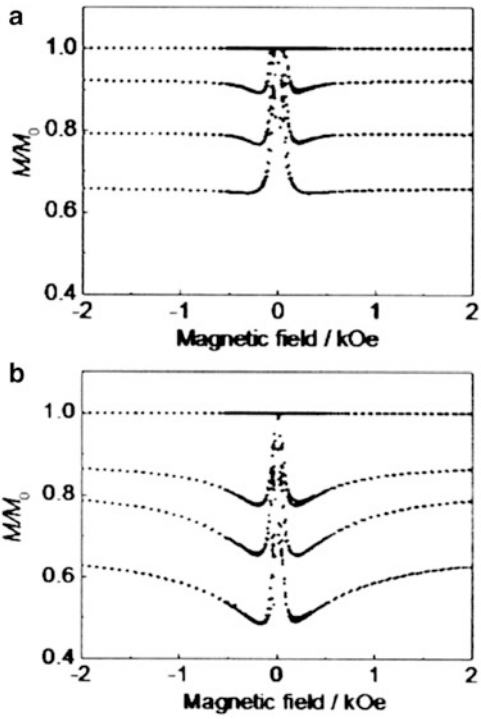

Fig. 8.15 Normalized magnetization for specimens of (I) 0 % porosity, (II) 11 % porosity, (III) 19 % porosity, and (IV) 35 % porosity in the low-magnetic field (**a**) parallel and (**b**) perpendicular to the pore growth direction (Reprinted with permission from [29] © 2008 American Institute of Physics)

between anisotropy and porosity. The n value decreased toward unity with increasing applied magnetic field. The relationship between the applied magnetic field and n is shown in Fig. 8.17. The n values take a maximum, approximately 1.8 (perpendicular) and approximately 1.1 (parallel) at around 200 Oe. The anisotropy of magnetization clearly appears when $n > 1.1$, i.e., magnetic field less than 2.3 kOe. The n values of 1.8 and 1.1 are coincident with those reported by Tane et al. [20] for electrical conductivity of lotus nickel in the parallel and perpendicular direction, implying the existence of remarkable similarity between electrical conductivity and magnetization.

A possible mechanism of the coincidence in n may come from similar spatial distribution of the electrical current and magnetic flux in the lotus nickel. When a low-magnetic field is applied, the magnetic anisotropy originates from the area of the pore walls perpendicular to the direction of applied magnetic field because magnetic poles created at the pore wall increase the total energy of the system, and therefore, this area acts as a resistance to magnetization. The anisotropic shape of pore is considered to cause the observed magnetic anisotropy, and at a low-magnetic field, the magnetic flux in lotus materials flows without crossing pore wall. Since electrical current also flows without crossing pore walls, the spatial distribution of electrical current and magnetic flux should be similar at a low-magnetic field, and similar values of n are expected to appear in electrical conductivity and magnetization.

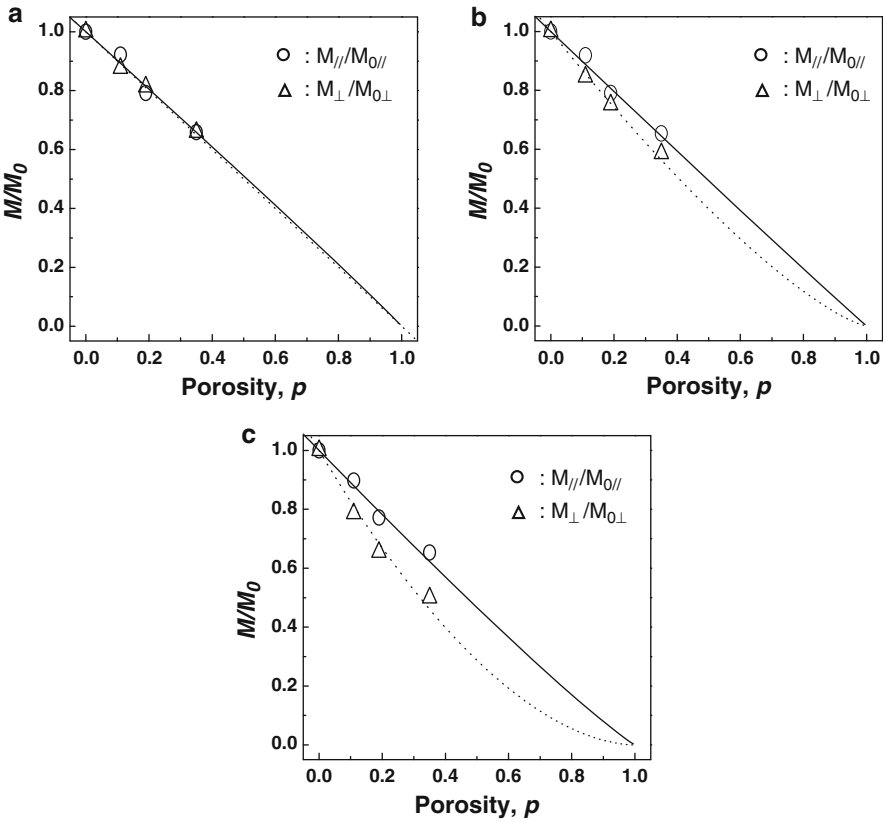

Fig. 8.16 Porosity dependence of the normalized magnetization at the magnetic field of (**a**) 10 kOe, (**b**) 1 kOe, and (**c**) 200 Oe. The *plots* indicate the experimental data, and the *lines* indicate the fitting results of formula (8.23) to the experimental data (Reprinted with permission from [29] © 2008 American Institute of Physics)

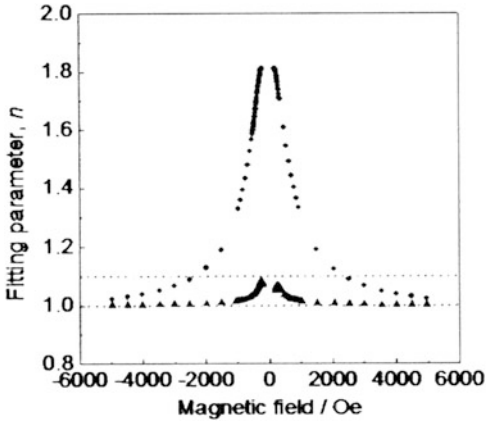

Fig. 8.17 Dependence of the fitting parameter n on magnetic field applied to parallel (*filled triangles*) and perpendicular (*filled circles*) to the pore growth direction. The *broken lines* indicate $n = 1$ (the case in which all the pores are penetrated) and $n = 1.1$ (10 % anisotropy at the point) (Reprinted with permission from [29] © 2008 American Institute of Physics)

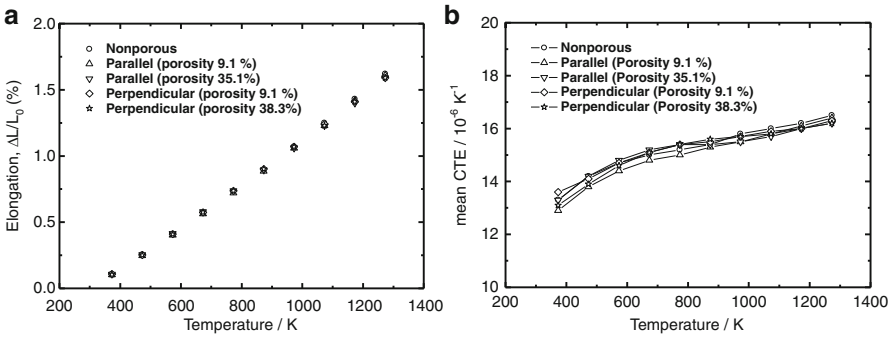

Fig. 8.18 (**a**) Elongation of lotus nickel in the direction parallel and perpendicular to the pore axis with different porosities as a function of temperature. (**b**) Coefficient of linear thermal expansion of lotus nickel in the direction parallel and perpendicular to the pore axis with different porosities as a function of temperature (Reprinted with permission from [31] © 2006 Elsevier Ltd)

8.5 Thermal Expansion

The understanding of the properties of thermal expansion of lotus-type porous metals is important for the practical application such as the electrode, heat sink, and high-temperature parts. Measurements of thermal expansion were carried out by Tane et al. [31] in a thermal dilatometer. The equipment uses an alumina pushrod in contact with the specimen to record the change in linear dimension during a heating. The samples were in the shape of rods of nonporous and porous nickel of 6 mm in diameter and 15 mm in length. The temperature was increased from 294 to 1,273 K at a rate of 1 K min^{-1}. Measurements were performed under mechanical-pump vacuum which was sufficient to prevent from oxidation, as verified by measuring negligible mass changes after the experiments.

The thermal expansion data for nickel samples with different porosities are shown in Fig. 8.18a, where $\triangle L = L - L_0$ and L_0 is the original length of samples at room temperature. In general, it is convenient to express the thermal expansion behavior by the coefficient of linear thermal expansion (CTE) as follows:

$$\alpha = \frac{1}{L_0}\frac{\Delta L}{\Delta T}, \tag{8.24}$$

where α is the coefficient of thermal expansion (K^{-1}), L_0 is the original sample length (m), and $\triangle T = T - T_0$ is the temperature interval ($T_0 = 293$ K). The values of CTE α for specific temperature ranges are shown in Fig. 8.18b. These results show no significant effect of the porosity and the pore direction in the lotus-type porous nickel on the CTE.

For prediction of the CTE of metal-matrix composite, the models are derived by Kerner [32] and Schapery [33]. Kerner's model gives the CTE of composite as

$$\alpha_c = \bar{\alpha} + V_p(1 - V_p)(\alpha_p - \alpha_m)\frac{K_p - K_m}{(1 - V_p)K_m + V_pK_p + (3K_pK_m/4G_m)}, \quad (8.25)$$

where $\bar{\alpha}$ is the rule-of-mixtures value given by $V_p\alpha_p + (1 - V_p)\alpha_m$. K and G are the bulk and shear moduli, V is the volume fraction, and α is the coefficient of thermal expansion. The subscripts c, p, and m denote composite, particle, and matrix, respectively.

The Schapery's model is written as

$$\alpha_c = \alpha_p + (\alpha_p - \alpha_m)\frac{(1/K_c) - (1/K_p)}{(1/K_m) - (1/K_p)}. \quad (8.26)$$

In the case of porous metals, the K_p in Eqs. (8.25) and (8.26) is zero and then $\alpha_c = \alpha_m$. This indicates the CTE of lotus-type porous metals depends on that of the matrix, which the effect of porosity on CTE can be neglected.

8.6 Corrosion

It is well known that the properties of passive films on stainless steels depend on the type of solution used for the corrosion tests. Stainless steels exhibit different corrosion resistance in alkaline, neutral, and acidic environments, since the mechanisms of formation and breakdown of the passive film are different [34]. AISI 316L stainless steel has been used as a surgical implant material for many years exhibiting sufficient corrosion resistance under body fluids which contain Cl^- ion as well as many other components such as water, dissolved oxygen, bacteria, cells, enzymes, and proteins. The improved corrosion resistance of type AISI 316L stainless steel in a chloride environment is attributed to the addition of molybdenum which is effective in stabilizing the passive film in the presence of chlorides [35]. Recently it has been found that nitrogen addition to austenitic stainless steel improves the pitting corrosion resistance [36–38]. In addition, nitrogen as an alloy component allows a nickel content reduction in the austenitic stainless steel, since the allergic reactions caused by this element is suppressed.

Potential applications of this new family of stainless steels include components subjected to corrosion and wear mechanisms, structural components, as well as medical and biocompatible parts, because nitrogen confers high-yield strength, ultimate tensile strength and ductility, as well as fracture toughness, low-magnetic permeability, very favorable localized corrosion resistance, and higher wear and abrasion resistance. Due to the combination of these excellent properties, currently there is also much interest in the fabrication of porous parts made of high-nitrogen Ni-free stainless steels.

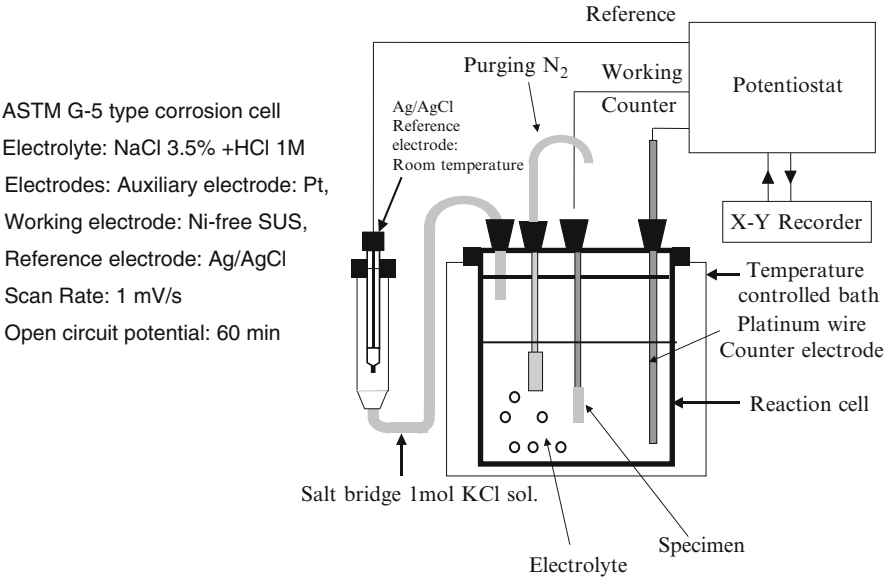

Fig. 8.19 Experimental setup for measurement of electrochemical polarization curves

The corrosion behavior of porous materials in general differs from that of the bulk materials of the same composition. Moreover, the pore morphology, porosity, pore size, and pore surface condition also interfere in the degradation process, in view of the fact that a porous material is attacked not only on its surface but also from inside. Alvarez et al. measured the corrosion rates, corrosion potentials, and breakdown potentials in dehydrogenized porous and nonporous specimens in order to investigate the corrosion resistance of lotus high-nitrogen Ni-free stainless steels and to compare it with the nonporous material [39].

Electrochemical polarization experiments were conducted using a potentiostat unit connected to a potential and current x–y recorder. The results were finally processed in a personal computer using a data acquisition program. The potentiodynamic polarizations were performed at a scan rate of 1 mV s^{-1}, and the scans were started at +100 mV with respect to the open-circuit potential. The details of the experimental setup are illustrated in Fig. 8.19.

The nitrogen effect in the polarization curves was examined firstly in nonporous samples. Potentiodynamic polarization curves for the nonporous nitrided and non-nitrided alloys are shown in Fig. 8.20, where the current density is a measure of the corrosion rate. It was confirmed that the nitrogen alloying suppressed the pitting corrosion even in such a low pH and high Cl^{-1} concentration solution. A more stable passivity region was established due to the nitrogen alloying. Moreover, the solution-nitrided samples exhibited lower passivation current I_{pass}. The breakdown potentials for all the solution-nitrided samples were found to be more noble than the non-nitrided samples, thus exhibiting improved corrosion resistance in 3.5 wt% NaCl + 1 M HCL. The high-pitting potential of high-nitrogen

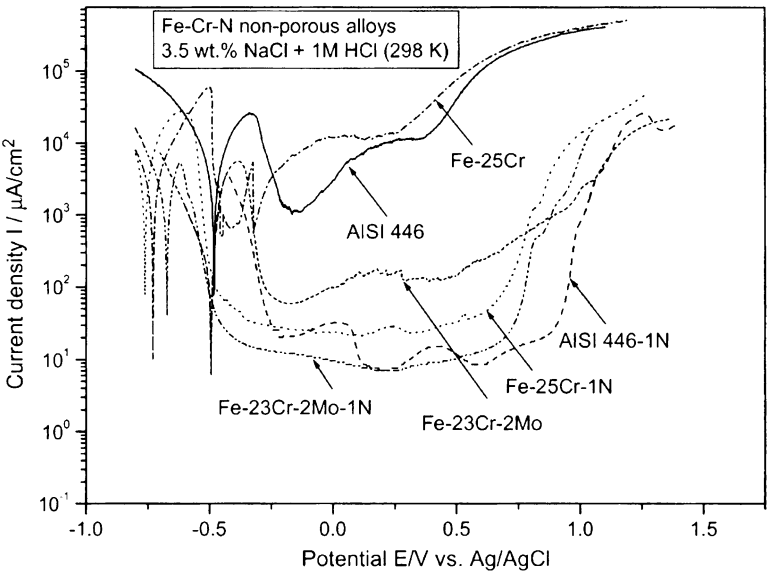

Fig. 8.20 Nitrogen alloying effect in the potentiodynamic polarization curves of the investigated samples (Reprinted with permission from [39] © 2007 Elsevier Ltd)

steels is attributed to the amount of N dissolved within the austenite. Together with a sufficient Cr and Mo content, which bring about a passive layer (Cr) and a pre-passive film (M), respectively, nitrogen leads to an increase of the pH value within the surrounding medium by a decomposition of NH_3 to $NH_4^+ + OH^-$ [40]. Indeed, Fe-23wt%Cr-2wt%Mo-1wt%N alloy resulted to have the higher corrosion potential. Inspection of the non-nitrided samples after polarization showed pitting in the surfaces of the AISI 316L and also in AISI 446 stainless steel and Fe-25wt%Cr, Fe-23wt%Cr-2tMo alloys, while in the solution-nitrided samples, the surface after the polarization looked only etched by the electrolyte.

When comparing results for the porous and nonporous alloys, in the former, a clear susceptibility to the attack of chloride ions was found. Figure 8.21 shows the polarization curves of the porous and nonporous solution nitride alloys. A clear defined passive region was not observed in the porous alloys; in contrast, the nonporous alloys exhibited a very wide passive region. The passive current was 2 orders of magnitude higher for the porous alloys than for nonporous alloys. Regarding the breakdown potential, the nonporous alloys exhibited a slightly more noble breakdown potential. The porous configuration could have introduced many small crevices which are conductive to localized corrosion, especially in the internal surface of the pores that cannot be mechanically polished. In these sites a marked increase in the acidity within a confined space could be able to accelerate localized corrosion.

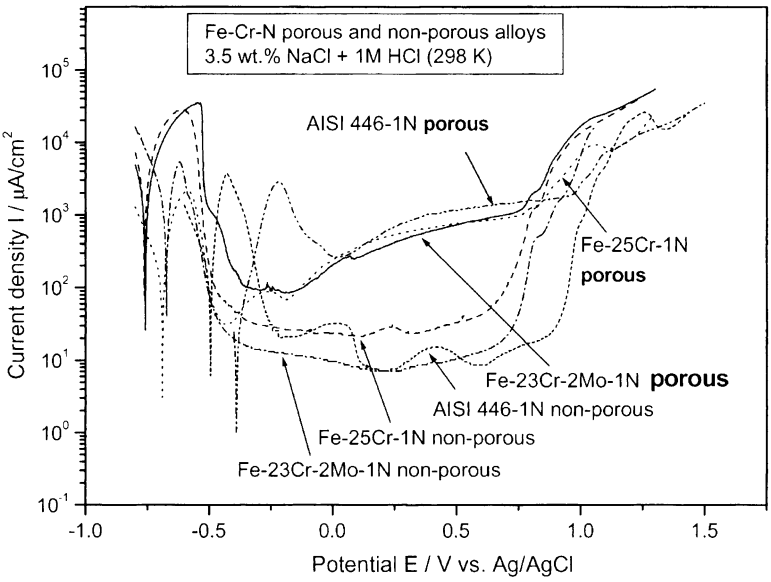

Fig. 8.21 Potentiodynamic polarization curves of lotus Fe-25wt%Cr-1wt%N, Fe-23wt%Cr-2wt% Mo-1wt%N, and AISI446-1wt%N steels and nonporous steels in 3.5wt%NaCl + 1 M HCl solution (Reprinted with permission from [39] © 2007 Elsevier Ltd)

Figure 8.22 shows the electropolishing effect in the porous specimens. This study revealed that solution nitriding + electropolishing produces a polarization curve with a very wide passive region. The current density in this passive region is within 14–300 μA cm^{-2}, almost as low as the nonporous samples' current density.

Therefore, a way of increasing the corrosion resistance of lotus alloys is to electropolish the porous surface in order to remove deformed layer, improve surface roughness, and also form a durable passive film on the surface. This more uniform oxide layer resulting from electropolishing will increase corrosion resistance in stainless steels. It is worth noting that the electropolishing treatment applied in the porous alloys did not alter the breakdown potential significantly. However, the passive current densities in the active–passive transition were greatly reduced and the passivating ability, given by the wide passivation range of the polarization curves, also increased by this final surface finish. These results indicate that a higher corrosion resistance is obtained after the electropolishing surface treatment.

The results of pitting corrosion susceptibility can also be interpreted using the images of the surface microstructure after corrosion obtained by scanning electron microscopy. Selected SEM micrographs of lotus nitrided alloys after the polarization test in 3.5wt%NaCl + 1 M HCl are shown in Fig. 8.23a–d. SEM observation revealed that lotus AISI 316L stainless steel experienced severe localized

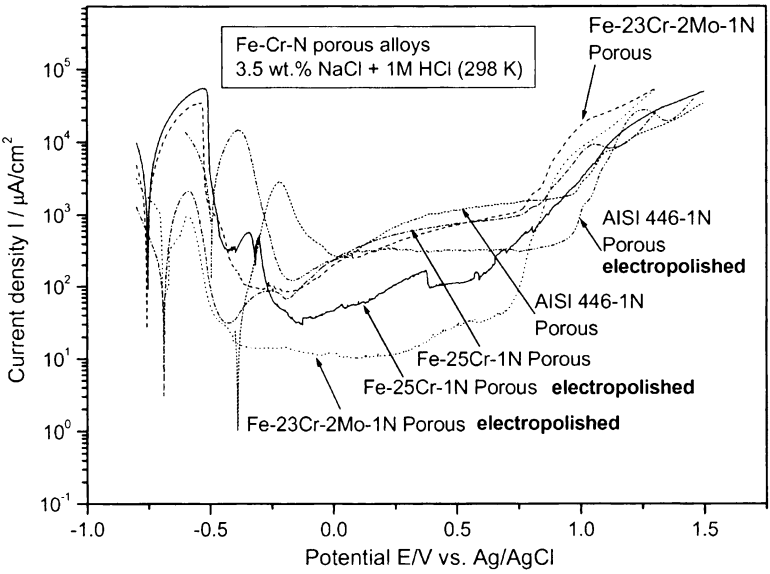

Fig. 8.22 Potentiodynamic polarization curves of lotus Fe-25wt%Cr-1wt%N, Fe-23wt%Cr-2wt%Mo-1wt%N, and AISI446-1wt%N steels with and without electropolishing using an electrolyte composed in phosphoric acid 56 %, sulphuric acid 27 %, glycerine 7 %, and DI water at 333 K (Reprinted with permission from [39] © 2007 Elsevier Ltd)

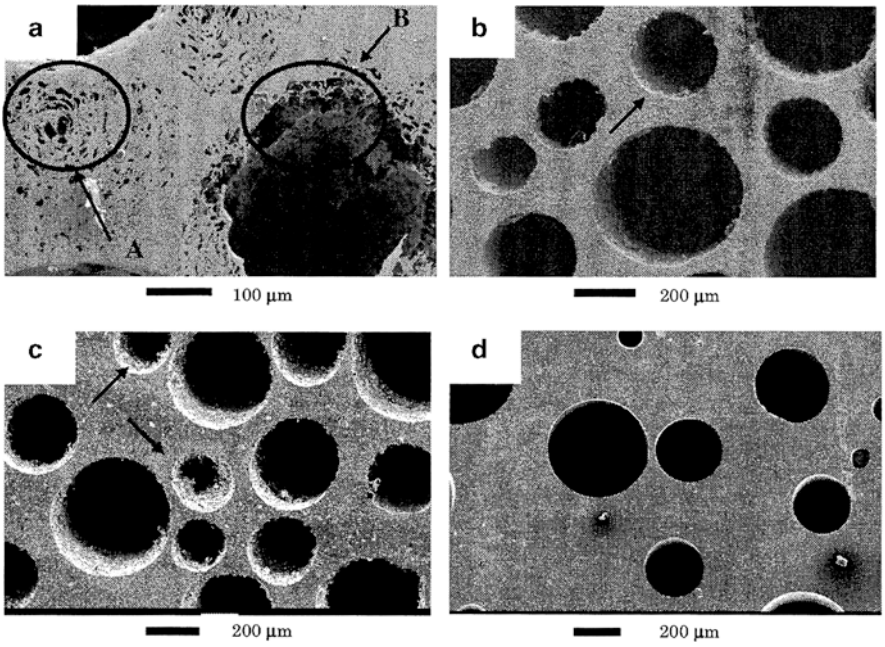

Fig. 8.23 SEM micrographs of the investigated lotus alloys after the polarization in 3.5wt% NaCl + HCl 1 N. (**a**) AISI316L, (**b**) Fe-25wt%Cr-1wt%N, (**c**) AISI446-1wt%N, and (**d**) Fe-23wt%Cr-2wt%Mo-1wt%N (Reprinted with permission from [39] © 2007 Elsevier Ltd)

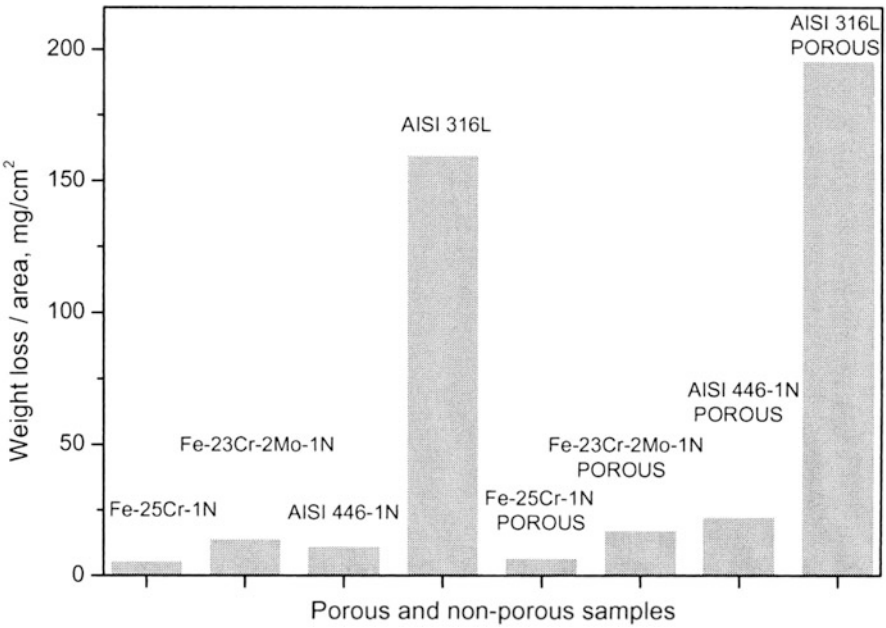

Fig. 8.24 Weight loss in 10wt%$FeCl_3 \cdot 6H_2O$ after 48 h immersion for the porous and nonporous high-nitrogen Ni-free stainless steels (Reprinted with permission from [39] © 2007 Elsevier Ltd)

corrosion. The metal base (zone A in Fig. 8.23a) as well as the internal surroundings of the pores (zone B in Fig. 8.23a) were attacked. The pits found in the metal base of AISI 316L consist of an open center, perforated middle region, and an outer ring. The center and the middle regions are typical perforated or "lacy" pit morphology in which subsurface undercutting expands the pit from the central initiation point. Contrastingly, no obvious corrosion pits were found in any of the high-nitrogen Ni-free alloys (Fig. 8.23b–d). In the case of Fe-25wt%Cr-1wt%N and AISI 446-1wt %N (Fig. 8.23b, c, respectively), it was observed that the internal wall of the pores, marked with arrows in Fig. 8.23b, c, seems to be degraded and not smooth like in the case of Fe-23wt%Cr-2wt%Mo -1wt%N Fig. 8.23d). This difference in the microstructure of the inner part of the pores in the high-nitrogen Ni-free stainless steels is probably because Fe-23wt%Cr-2wt%Mo-1wt%N alloy exhibited the lower corrosion rate under the experimental conditions. These results confirm the higher corrosion susceptibility of AISI 316L compared to high-nitrogen Ni-free stainless steels. In every high-nitrogen Ni-free alloy investigated, severe open perforated pit structure was not observed after the polarization test.

The results after immersion test in 10wt%$FeCl_3 \cdot 6H_2O$ solution for 172.8 ks are shown in Fig. 8.24. It was observed that lotus AISI 316L exhibited the highest weight losses. Metallographic observations revealed that AISI 316L stainless steel coupons displayed much more pits than the rest of the solution nitride samples. Moreover, the pits developed on AISI 316L were wider and deeper with average

size of 100 μm for the nonporous specimen and 150 μm for the lotus specimen. On the contrary the high-nitrogen Ni-free stainless steel specimens after 172.8 ks immersion showed a very smooth and bright surface with a small number of shallow pits with a diameter not exceeding 20 μm. The corrosion rate determined by weight loss method of the high-nitrogen Ni-free stainless steel specimens in this highly oxidizing chloride environment was less than 0.04 mm y^{-1}. In contrast, AISI 316L stainless steel-corroded samples showed a very high average corrosion rate. Corrosion rate of duplicate runs determined by weight loss method showed average values of 0.86 and 1.52 mm y^{-1} for nonporous and lotus AISI 316L stainless steel, respectively. Therefore, it can be concluded that lotus high-nitrogen Ni-free stainless steels possess the general corrosion resistance much better than conventional austenitic stainless steels in acidic chloride environment.

The results of this investigation showed that the general corrosion resistance as well as the localized corrosion resistance of lotus high-nitrogen Ni-free stainless steels is higher than AISI 316L. From the microscopic observation and the electrochemical characterization, the alloy with best performance was lotus Fe-23wt%Cr-2wt%Mo-1wt%N since it resulted to be immune to pitting attack under these testing conditions. From the weight loss measurements, lotus Fe-25wt%Cr-1wt%N alloy tolerated very good the immersion in the severe aggressive media much better than any other alloy.

References

1. Xie ZK, Ikeda T, Okuda Y, Nakajima H (2004) Mater Sci Eng A 386:390–395
2. Xie ZK, Ikeda T, Okuda Y, Nakajima H (2004) Jpn J Appl Phys 43:7315–7319
3. Xie ZK, Ikeda T, Okuda Y, Nakajima H (2004) Mater Sci Forum 449–452:661–664
4. Kimura S (1977) Architectural sound and anti-noise plan. Shokokusha Publishing, Tokyo, p 142 (in Japanese)
5. Xie ZK, Ikeda T, Okuda Y, Nakajima H (2003) J Jpn Inst Metals 67:708–713
6. Okuda Y (1990) Proc J Acoustic Soc Jpn 581
7. Akiyama S, Itoh M, Ishii E (1991) National Industrial Research Institute. Report of Kyushu, p 2928
8. Nisimaki S (1971) Electro-acoustics and vibration. Corona Publishing, Tokyo, Japan, p 79
9. Beranek LL (1950) Acoustic measurement. Wiley, New York
10. Igarasi J (1970) Sound and vibration. Kyoritsu Shuppan Co., Tokyo, p 37
11. Behrens E (1968) J Compos Mater 2:2–17
12. Perrins WT, McKenzie DR, McPhedran RC (1979) Proc Roy Soc London Ser 369:207
13. Han LS, Cosner AA (1981) J Heat Transfer 103:387–392
14. Sangani AS, Yao C (1988) Phys Fluids 31:2435–2444
15. Mityushev V (1999) Proc Roy Soc London A 455:2513–2528
16. Moctezuma-Berthier A, Vizika O, Adler PM (2002) Trans Porous Media 49:331–332
17. Ogushi T, Chiba H, Nakajima H, Ikeda T (2004) J Appl Phys 95:5843–5847
18. Hyun SK, Murakami K, Nakajima H (2001) Mater Sci Eng A 299:241–248
19. Suematsu Y, Hyun SK, Nakajima H (2004) J Jpn Inst Metals 68:257–261
20. Tane M, Hyun SK, Nakajima H (2005) J Appl Phys 97:103701-1–103701-4
21. Tane M, Ichitsubo T (2004) Appl Phys Lett 85:197–199
22. Archie GE (1942) Trans AIME 146:54–63

23. Eshelby JD (1957) Proc Roy Soc London A 241:376–396
24. Mori T, Tanaka K (1973) Acta Metall 21:571–574
25. Hatta H, Taya M (1986) J Eng Mater 24:1159–1172
26. Ohnishi Y, Hyun SK, Nakajima H (2006) In: Nakajima H, Kanetake N (eds) Porous metals and metal foaming technology. Jpn Inst Metals, Sendai, pp 423–426
27. Noudem JG, Reddy ES, Schmitz GJ (2003) Physica C 390:286–290
28. Castano FJ, Nielsch K, Ross CA, Robinson JWA, Krishnan R (2004) Appl Phys Lett 85:2873–2875
29. Onishi H, Hyun SK, Nakajima H, Mitani S, Takanashi K, Yakushiji K (2008) J Appl Phys 103:093539
30. Igarashi H, Okazaki K (1976) J Am Ceram Soc 59:371–372
31. Tane M, Hyun SK, Nakajima H (2006) Scr Mater 54:545–552
32. Kerner EH (1956) Proc Phys Soc London B 69:808–813
33. Schapery RA (1968) J Comp Mater 2:380–404
34. Dillon CP (1995) Corrosion resistance of stainless steels. Marcel Dekker, New York, p 258
35. Seah KHW (1993) Corros Sci 34:1841–1851
36. Fossati A, Borgioli F, Galvaneto E, Bacci T (2006) Corros Sci 48:1513–1527
37. Di Schino A, Barteri M, Kenny JM (2003) J Mater Sci 38:4725–4733
38. Rechsteiner A, Speidel M (1997) Proceedings of 1st European stainless steel conference, vol 2, Florence, p107
39. Alvarez K, Hyun SK, Tsuchiya H, Fujimoto S, Nakajima H (2008) Corros Sci 50:183–193
40. Ernest P, Laycock NJ, Moayed MH, Newman RC (1997) Corros Sci 39:1133–1136